https://doi.org/10.5194/wes-2025-2
Preprint. Discussion started: 11 February 2025

eawe european academy of wind energy
Open Access WIND ENERGY SCIENCE DISCUSSIONS

Novel CFD approach for simulation of an ABL wind tunnel flow: validation and application to a FOWT model

Dimas Alejandro Barile[1,2], Roberto Sosa[1,3], Sandrine Aubrun[4], and Alejandro Daniel Otero[1,2]

[1]Universidad de Buenos Aires, Facultad de Ingeniería, Av. Paseo Colón 850, Buenos Aires, C1063ACV, Argentina
[2]CONICET, Centro de Simulación Computacional para Aplicaciones Tecnológicas, Godoy Cruz 2390, Buenos Aires, C1425FQD, Argentina
[3]CONICET - INTECIN, Av. Paseo Colón 850, Buenos Aires, C1063ACV, Argentina
[4]Nantes Université, École Centrale Nantes, CNRS, LHEEA, UMR 6598, F-44000 Nantes, France

Correspondence: Alejandro Daniel Otero (aotero@fi.uba.ar)

Abstract. When comparing Large Eddy Simulations with wind tunnel experiments, choosing the appropriate boundary conditions is crucial to ensure an accurate representation of wind flow. This becomes particularly challenging for Atmospheric Boundary Layer (ABL) wind tunnels, which frequently incorporate calibrated obstacles to replicate the appropriate model-scale ABL flow. Although many researchers prefer to include these elements within the CFD domain, this approach leads to high computational costs and the necessity for precise replication of each obstacle. Alternatives to avoid this high computational cost typically include slip boundary conditions at the top, leading to fast decay in turbulence quantities near the ground. In this study, the authors propose a new methodology based on the precursor technique, which is commonly used for full-scale ABL simulations, combined with a stress top boundary condition. The method is validated against experimental measurements showing significant improvement in the inlet flow quality, when compared to previous methods.

Floating Offshore Wind Turbines (FOWT) are expected to experience significant growth in the coming decades. However, due to the effect of platform motions, their wake structures can be challenging to predict. As a second part of this study, the novel technique is applied together with an actuator disk to represent an oscillating wind turbine model, designed to study FOWT wakes. Simulations with varying turbulence intensities and motion frequencies are conducted. The results corroborate previous findings that the near wake is not significantly influenced by surge motion frequency, although certain frequency cases exhibit more persistent coherence structures than others, which results in a slower wake recovery. This phenomenon is found to be less significant in the context of higher turbulence intensities.

1 Introduction

Atmospheric Boundary Layer (ABL) wind tunnels represent an excellent research and validation tool for the study of wind turbine wakes and wind farms. The capacity to reproduce wind turbine wakes at a reduced scale while preserving atmospheric flow characteristics has significantly advanced knowledge related to wake modelling, wind farm interactions, wind farm blockage, and other related topics. At the same time, precise Computational Fluid Dynamics (CFD) simulations of ABL wind tunnels offer significant support for advancing these studies further. However, generating the appropriate flow with a Large Eddy Sim-

https://doi.org/10.5194/wes-2025-2
Preprint. Discussion started: 11 February 2025

ulation (LES) scheme poses a challenge on its own. Many authors have adopted the concept of a Digital Wind Tunnel, where all the elements present in the physical wind tunnel are modeled in the simulation with high detail (Yi et al., 2024; Thordal et al., 2020; Feng et al., 2019; Wang et al., 2018; Lopez et al., 2016). While this approach yields the most accurate results, it is associated with a high computational cost and requires extensive knowledge of the facility. Another option to generating turbulence that is compatible with an ABL profile in the simulation is the use of Synthetic Turbulence models, which, despite recent advances, still fail to capture the largest scales present in the flow (Munters et al., 2016; Porté-Agel et al., 2020). To address this issue, many researchers over the last decade have employed periodic Boundary Conditions (BC) to reach a converged ABL flow, known as the precursor technique (Shi et al., 2016; Nandi and Yeo, 2021; Gao et al., 2021).

At real scale, the Atmospheric Surface Layer (ASL) refers to the lowest 10% of the ABL, where turbulent quantities and fluxes vary by less than 10% from their average values (Richards and Hoxey, 1993; Stull, 2012). This means that within the first 100–300 meters, these quantities display near-constant behaviour. Although there remain several open questions regarding the phenomena occurring within the ABL, significant progress has been made in recent years by using LES combined with a method that includes a 1 km-high domain, an inversion capping layer between 400 m and 800 m, depending on ABL stability and whether it is an onshore or offshore ABL, and a precursor technique, among other details (Churchfield et al., 2012a, b; Navarro Diaz et al., 2023). To reduce the computational domain height, Zahn and Bou-Zeid (2024) proposed a calibrated stress BC at the top of the reduced domain, as an alternative to the typical slip BC. The calibration process was developed by running a full ABL simulation and extracting the corresponding shear velocity at the height of the shorter domain, which afterwards was used into the BC. This approach effectively generated similar velocity and turbulence profiles without simulating the entire ABL, avoiding the rapid decay in turbulence variables that occurs when using a slip BC in combination with a truncated domain. Before that, O'Sullivan et al. (2011) and Jimenez et al. (2007) had succesfully employed a top stress BC for full scale simulation in RANS and LES, respectively. In both cases the shear velocity was obtained from a log law model based on surface roughness instead of a calibration process, though in the first case a fixed velocity gradient based on shear velocity was imposed as top BC while in the second a stress BC also based on shear velocity was imposed.

For ABL wind tunnel CFD simulations, most studies choose a geometric scale in order to include the entire ABL employing a slip BC at the top, which results in the rapid decay in turbulence variables (Shi et al., 2016; Nandi and Yeo, 2021; Calaf et al., 2010; Porté-Agel et al., 2000). The objective of this work is to represent, through LES simulations, an atmospheric wind tunnel located at École Centrale Nantes, where Schliffke et al. (2020); Belvasi et al. (2022); Schliffke et al. (2024) have focused on reproducing the ASL. In order to achieve this, we combine a pseudo-periodic BC at the inlet (Chen et al., 2022), which acts as a precursor, with a novel stress BC at the top, based on the shear velocity characteristic of the Centrale Nantes wind tunnel. This simulation scheme allows for the correct representation of the ABL profile characteristics of the wind tunnel while reducing the simulation domain.

Floating offshore wind turbines (FOWT) are proposed as main players of the next generation of wind farms due to the great offshore wind energy potential around the world. These turbines are subjected to 6 degrees of freedom movements, making it a challenge to correctly predict aerodynamics and wake characteristics. Many studies have been conducted in the last decade (Li and Yang, 2024; Wang et al., 2023; Bayati et al., 2017; Tran and Kim, 2016; Farrugia et al., 2016), both experimental and

https://doi.org/10.5194/wes-2025-2
Preprint. Discussion started: 11 February 2025

numerical, showing the impact on wake characteristics of the turbine motion. The majority of these studies were conducted under uniform inflow conditions and concluded that surge motions generate periodic expansion and contraction in the wake structure (Sivalingam et al., 2018; Lee and Lee, 2019; Chen et al., 2021; Hubert et al., 2024). Also, rigid movements facilitate the mixing process for low turbulence intensity (TI) cases, thus aiding wake recovery process (Li and Yang, 2024; Messmer et al., 2024; Li et al., 2022; Ramos-García et al., 2022). The situation is different when considering ABL flows, where very little number of studies were carried out to this days.

Johlas et al. (2019, 2020) conducted full ABL simulations with low TI ($\approx 4\%$), incorporating the motions induced by waves on a floating offshore wind turbine (FOWT). The results demonstrated that, due to pitch motion, the wakes of FOWTs exhibit an upward deflection in comparison to the wakes of fixed wind turbines. Also, Xu et al. (2023) combined surge and pitch motion for a FOWT, thereby confirming previous findings for wake center deflection and concluding that platform motions have negligible impact on wake recovery. In terms of experimental research, Schliffke et al. (2020, 2024) conducted experiments in an ABL wind tunnel with a porous disk subjected to surge motion and analysed wake profile 4.6D downstream. They did not find significant differences on wake flow statistics between motion frequencies, although they where able to identify the signature of movement frequency in the wake velocity spectra. Fontanella et al. (2022) obtained analogous results regarding wake recovery in an ABL wind tunnel by analysing the wake at 2.3D with low TI. To date, there has been a notable absence of research exploring the effects of high TI on FOWT. Although offshore wind conditions tend to fall into the low to mid TI values (Barthelmie et al., 2005), high TI up to 10%-12% have been observed during specific periods (Bodini et al., 2020). Consequently, the authors in this work aim to address this knowledge gap by numerically analysing a wind turbine scale model subjected to surge motions with different frequencies and ABL flow, with medium and high turbulence. To this end, the CFD approach developed is combined with an adaptive actuator disk (AD) model that allows rigid motion representation into a LES solver.

The paper will be organised as follows: the wind tunnel facility used for cross-comparison is detailed in section 2, along with the numerical setup and the new BC. Section 3 presents the results regarding the new BC and validation against experimental measurements. Sections 4 and 5 show the wakes of the AD subjected to surge motion and wake recovery analysis, respectively. Finally, conclusions are drawn in section 6.

2 Experimental and Numerical Setup

2.1 ABL wind tunnel

The wind tunnel measurements used for validation were obtained in the ABL wind tunnel located at École Centrale Nantes. This open-circuit atmospheric wind tunnel has a 26-metre long test section and a 2 m $\times$ 2 m cross-section. The geometric scale was chosen to be 1:500. This facility was employed to study a porous disk subjected to motion with varying degrees of freedom with the objective of modelling and analysing FOWT wakes. The disk center height (H) is 0.12 m and its diameter (D) is 0.16 m. For further details on the experimental set-up, see Schliffke et al. (2024).

https://doi.org/10.5194/wes-2025-2
Preprint. Discussion started: 11 February 2025

2.2 Governing equations

For this work, a new solver was developed in OpenFOAM (OpenCFD-Ltd, 2004) based on SOWFA Libraries (Churchfield et al., 2012a, b). Among the modifications to the original solver, the driving pressure gradient was retained setting a target average velocity at a designated height but considering only a portion of the domain, which is not affected by the disk wake, for the calculation. Additionally, temperature effects were neglected. The spatial filtered incompressible Navier–Stokes equation of continuity (equation 1) and momentum conservation (equation 2) are solved,

$$\frac{\partial \tilde{u}_i}{\partial x_i} = 0, \tag{1}$$

$$\frac{\partial \tilde{u}_i}{\partial t} + \frac{\partial}{\partial x_j}(\tilde{u}_j \tilde{u}_i) = -\frac{\partial \tilde{p}}{\partial x_i} - \frac{1}{\rho_0}\frac{\partial p_0}{\partial x_i} - \frac{\partial \tau_{ij}}{\partial x_j} - \frac{1}{\rho_0} f_i, \tag{2}$$

where $\tilde{u}_i$ denotes the resolved filtered velocity component, with $i = 1,2,3$, corresponding to the streamwise, crosswise and vertical ones, respectively. Also $\tilde{p}$ is the modified pressure, τ_{ij} is the deviatoric part of the stress tensor which includes subgrid stress modeled by a one-equation eddy viscosity approach (Yoshizawa, 1986), and f_i stands for the AD forces. The second term in the right-hand side stands for the pressure gradient driving the flow.

2.3 Stress BC

Replicating the procedure proposed by Zahn and Bou-Zeid (2024) a stress BC based on the shear velocity is set at the top of the domain. Here, instead of a calibration process with a larger domain, the shear velocity is set according to the ABL wind tunnel profile reported by Schliffke et al. (2024). Considering a logaritmic law fitting

$$U = \frac{u_*}{\kappa}\left[ln(\frac{z}{z_0})\right], \tag{3}$$

the authors have determined the following parameters: $z_0 = 1.15 \times 10^{-5} m$ and $u_* = 0.12 ms^{-1}$. Then, at the top of the domain, the applied stress results in:

$$\tau_{xz} = u_*^2. \tag{4}$$

2.4 Actuator disk

An AD approach (Diaz et al., 2019; Navarro Diaz et al., 2019, 2021; Navarro Diaz et al., 2023) is applied to model the effect of the porous disk, which is assumed to have a constant thrust coefficient (Aubrun et al., 2019). First, a calibration table is constructed, for which the motionless AD is simulated with different fixed inlet wind speeds and uniform force distribution, in order to establish the induction relation between the unperturbed wind speed and the velocity at the disk plane. The AD is composed by nodes arranged along rings as illustrated in figure 1, where the radial position for each AD node is denoted as r_i.

https://doi.org/10.5194/wes-2025-2
Preprint. Discussion started: 11 February 2025

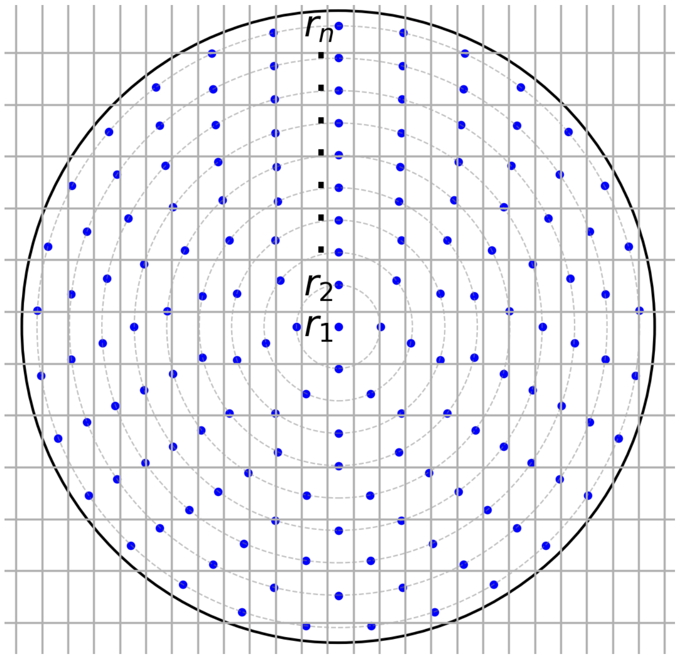

Figure 1. Schematic of the AD nodes arranged in rings, and the background CFD mesh.

The separation between rings is set according to Navarro Diaz et al. (2023). During the calibration process, the nodal force for each AD node is calculated as

$$\Delta f_i = \frac{1}{2}\rho\, C_t\, {U_\infty}^2\, \Delta S_i, \tag{5}$$

120 where U_∞ is the inlet velocity, ρ is the air density, C_t is the disk thrust coefficient, ΔS_i is the disk area corresponding to the particular AD node. For each node r_i, U_∞, the local velocity U_i, and local force f_i are recorded in table 1. Subsequently, during the simulation, in each time step, the local fluid velocity in each AD node is added to the rigid motion velocity in order to obtain the corresponding U_i sensed in the node. The force on AD node i is then calculated by interpolation from table 1 using r_i and U_i.

125 As described by Navarro Diaz et al. (2023), the AD is constituted by nodes on a plane disk that are not associated with the fluid mesh, as shown in figure 1. In order to assure numerical stability, the forces calculated at each node are subsequently distributed across the adjacent cells using a regularization kernel, which employs a three-dimensional Gaussian function (Porté-Agel et al., 2011; Hodgson et al., 2021).

2.5 Computational Domain dimensions and BCs

130 In order to evaluate the efficacy of the new BC in comparison to the classical slip BC, two domains are built. Both of them are 175D long and 10D wide, and the height for the slip BC domain is 15D while the height for the stress BC domain is 5D. A schematic of the final mesh for the latter is presented in figure 2. D and H, and correspondingly the D/H ratio, are identical

https://doi.org/10.5194/wes-2025-2
Preprint. Discussion started: 11 February 2025

Table 1. Calibration table for calculating nodal forces. In each node the value is obtained from the table by interpolating with r_i and the local velocity U_i.

Inlet Velocity	Radial Position	Local Velocity	Local Force
	r_1	U_1	f_1
$U_{\infty 1}$	$\vdots$	$\vdots$	$\vdots$
	r_n	U_n	f_n
	r_1	U_{n+1}	f_{n+1}
$U_{\infty 2}$	$\vdots$	$\vdots$	$\vdots$
	r_n	$U_{n\cdot 2}$	$f_{n\cdot 2}$
$\vdots$	$\vdots$	$\vdots$	$\vdots$
	r_1	$U_{n\cdot(m-1)}$	$f_{n\cdot(m-1)}$
$U_{\infty m}$	$\vdots$	$\vdots$	$\vdots$
	r_n	$U_{n\cdot m}$	$f_{n\cdot m}$

to those adopted in Schliffke et al. (2020, 2024). Both cases are configured with an inlet BC mapped from the section at 75D, highlighted in yellow in figure 2. This functions as a precursor, generating a continuous inlet ABL flow without the necessity of saving the precursor run. A starting mesh with 3.2 cells$/D$ in horizontal direction and 12.8 cells$/D$ in vertical direction is constructed. A mesh gradient is set in the vertical direction in order to ensure an accurate representation of the flow near the ground, and for the stress BC case this cell size gradient is also added at the top of the domain. Once the precursor reaches a converged flow, a mesh refinement is carried out in two steps. First, $25D$ downstream from the section where the inlet is mapped all cells within a box $3D$ wide and $2.5D$ high are divided by four in each horizontal direction. Then, at 25D downstream from the first mesh refinement, the cells within a box $2.5D$ wide and $1.9D$ high are divided by two in each horizontal direction. This results in 25.6 cells per diameter at 125D from the beginning of the domain with the cell size maintained at this level until the end of the domain. The test section is situated at 25D downstream from the second mesh refinement. The overall mesh for the *stress BC* consist of 4.84M cells, while the original *slip BC* consists of 6.99M cells, representing a reduction of 31% in the number of cells thanks to the stress BC, which directly reflects on the computational cost.

Periodic BCs are set in both lateral sides. For the *stress BC* case, stress BC is set at the bottom, based on Schumann's model (Schumann, 1975), and at the top based on the shear velocity, as previously described in 2.3. Both are highlighted in orange in figure 2. A second case is also built by reducing the roughness z_0 to a 10% of the value reported in Schliffke et al. (2024) and adjusting the corresponding shear velocity at the top in order to produce a lower TI case. For the *slip BC* case, the same BC is applied at the bottom but only the higher TI case is constructed for comparison. A longitudinal pressure gradient is configured to maintain the average velocity value at $z = H$. However, only the precursor part of the domain is taken into account for

https://doi.org/10.5194/wes-2025-2
Preprint. Discussion started: 11 February 2025

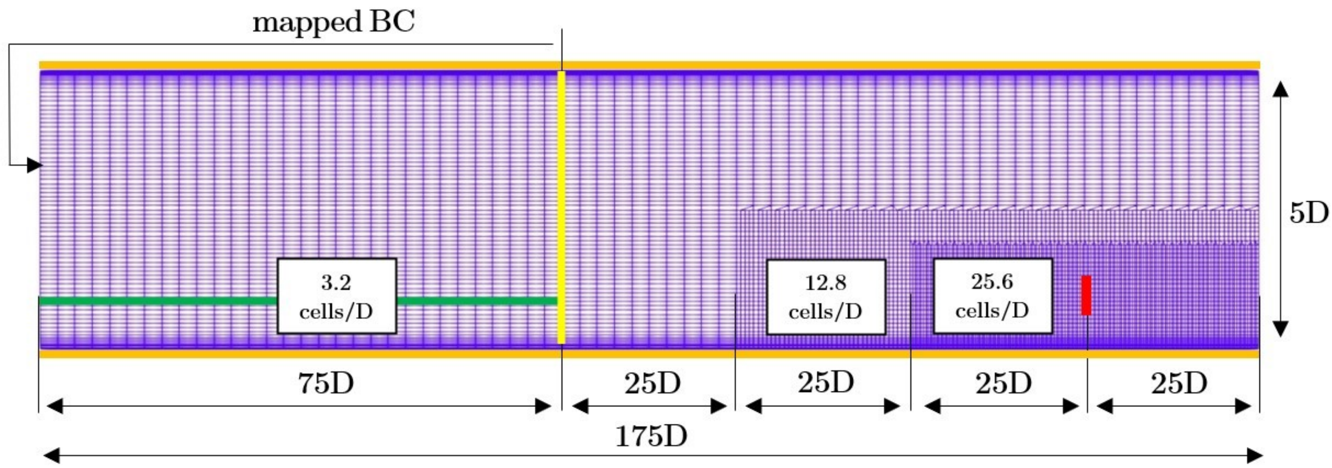

Figure 2. Mesh schematic for the *stress BC* case. The mapped section for the inlet BC is marked in yellow. The cells used for pressure gradient calculations are highlighted in green. The AD is shown in red and the stress BCs are applied in the orange zones.

the calculation of this average velocity in order to avoid contamination by the disk wake, as identified in green in figure 2. Subsequently, this force is applied to the entire domain.

The precursor is run for 1200 s, after which mesh refinement is carried out and the AD force is applied while maintaining the pressure gradient. The next 30 s of simulation are discarded in order to allow the corresponding wake structures to develop, after which the following 30 s are analysed.

A sinusoidal surge motion is applied to the AD,

$$\Delta x(t) = A_{surge}\, sin(2\pi f_{surge}\, t), \tag{6}$$

where the amplitude A_{surge} is set to $D/8$ and a range of frequencies f_{surge} from 0 Hz to 5.5 Hz are applied to the disk movement, following the experiments carried out by Schliffke et al. (2020, 2024). Table 2 summarizes the cases run, with their reduced frequency defined as:

$$f_{red} = \frac{f \cdot D}{U_{ref}} \tag{7}$$

In each case, U_{ref} is defined as the mean velocity at hub height without the AD.

3 Experimental validation

We start by analysing the average velocity and turbulent kinetic energy (TKE) profiles for the *slip BC* case and the *stress BC* case after the precursor run. The results are presented in figure 3. According to Zahn and Bou-Zeid (2024) when a stress BC is used the top 20% of the domain should be excluded from the analysis. Then, we compare the profiles up to 4D. It can be seen

https://doi.org/10.5194/wes-2025-2
Preprint. Discussion started: 11 February 2025

Table 2. Cases analysed and the respective surge and reduced frequency. The value U_{ref} used for f_{red} calculation is measured at hub height from the run without AD.

Surge frequency	f_{red}	TI	case id
0 Hz	0	Low	`LT-000`
		High	`HT-000`
2 Hz	0.11	Low	`LT-011`
		High	`HT-011`
3 Hz	0.17	Low	`LT-017`
		High	`HT-017`
4 Hz	0.23	Low	`LT-023`
		High	`HT-023`
5 Hz	0.29	Low	`LT-029`
		High	`HT-029`
5.5 Hz	0.31	Low	`LT-031`
		High	`HT-031`

that velocity profiles between both cases with higher TI (`HT`) match perfectly below 4D, but the stress BC avoids the steady decrease in TKE values produced by the slip BC, showing a recovery in TKE for greater heights. It can be clearly observed that the method successfully helps maintain the ASL turbulence closer to a profile with small variations around an average value, as it should be, compared to the traditional slip BC. Additionally, both figures show the outcomes for the lower TI (`LT`) *stress BC* case. While the velocity profile exhibits a strong correlation with previous ones, which is also confirmed near the ground in the detailed semi-log view of figure 3 (center), the TKE is comparatively lower than in the higher TI case.

In order to validate the developed flow that will interact with the AD, after mesh refinement, the average velocity and TI results are plotted along with the values reported in Schliffke et al. (2024), in figure 4. The velocity profile, zoomed in the refined region around the AD, is presented for all cases along with the logarithmic fit computed by the authors from the wind tunnel measurements. Both `HT` and `LT` velocity profiles show a high degree of correlation with the reported values. Regarding the TI for each velocity component, it can be observed that both cases have an overall good agreement with experimental values from Schliffke et al. (2024). The `HT` case demonstrates a surplus in all three components whereas the `LT` case exhibits a great match across all three, with slight surplus observed in the U component. When comparing the *slip BC* with the `HT` case, all three components exhibit a decline in TI with increasing height. This phenomenon is addressed by the novel methodology implemented. Besides, a higher computational cost is required by the last case.

Finally, resolved TKE and Reynolds stress $< u'_x u'_z >$ profiles in the flow that will interact with the AD are shown in figure 5. As previously observed, a considerably faster decay with height in the *slip BC* can be seen for both profiles when comparing with the *stress BC* `HT` case. Regarding the *stress BC* `LT`, it shows a similar behaviour than the `HT` case, besides the evident difference in values due to TI set-up. The two plots include experimental values from Schliffke (2022), which correspond to

https://doi.org/10.5194/wes-2025-2
Preprint. Discussion started: 11 February 2025

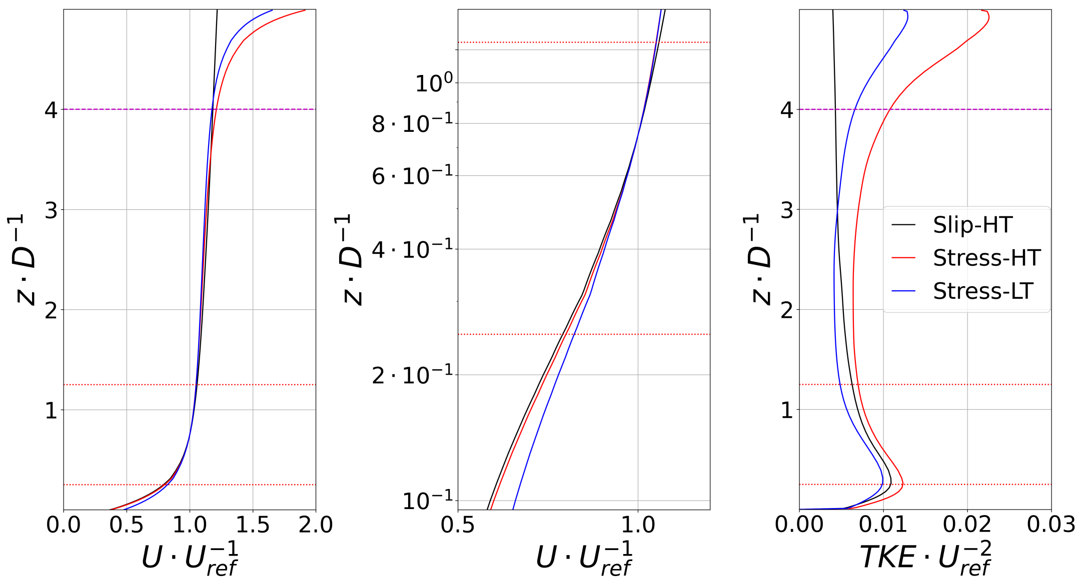

Figure 3. Vertical profiles after the precursor run: inlet flow average velocity on a linear scale (left), and zoomed on a semi-logarithmic plot (center). Resolved TKE is also included (right). Red dotted lines enclose the AD region.

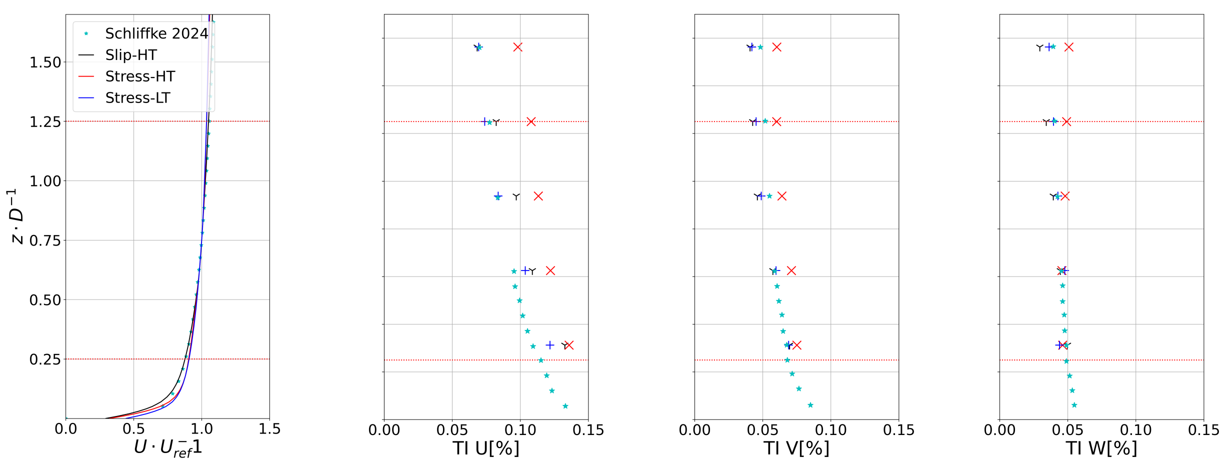

Figure 4. Inlet flow average velocity and TI profiles for 3 velocity components after mesh refinement for the *Stress BC* cases, `LT` and `HT`, and the *slip BC* case `HT`. All profiles are zoomed in the refined region and compared with experimental values from Schliffke et al. (2024).

https://doi.org/10.5194/wes-2025-2
Preprint. Discussion started: 11 February 2025

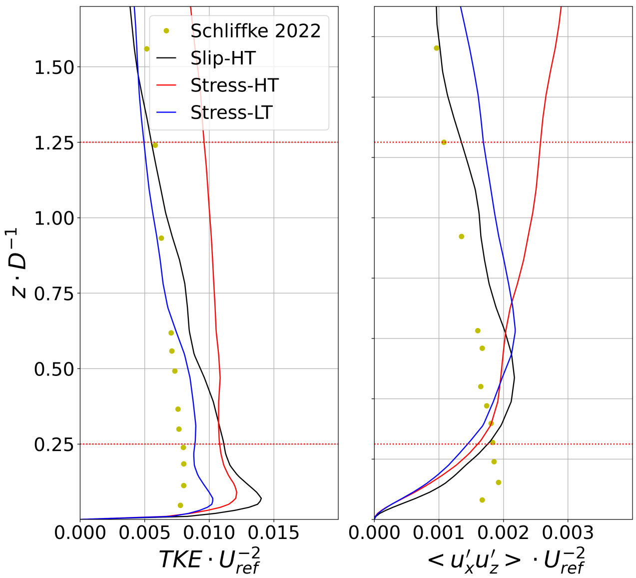

Figure 5. Inlet flow average TKE (left) and Reynolds stress $< u'_x u'_z >$ (right) profiles after mesh refinement. All profiles are zoomed in the refined region and compared with experimental values from Schliffke (2022), corresponding to the same experiment as figure 4.

the same study as the results shown in figure 4. Once more, the LT case demonstrates greater alignment with experimental values, showing a notable correlation in the TKE profile and a satisfactory representation for $< u'_x u'_z >$. The results confirm that the method has been effective in replicating the wind tunnel ABL flow profile.

4 Wakes of the AD under surge motion

As a first visualization of the wake, figure 6 displays instantaneous velocity fields downstream the AD for the HT and LT cases. For reduced frequencies of 0.23, 0.29 and 0.31, the LT cases show a more defined wake structure with expansion and contraction of wake diameter as it was reported by Sivalingam et al. (2018); Lee and Lee (2019); Chen et al. (2021); Hubert et al. (2024). On the other hand, the effect is less evident for the HT cases, where some pattern appears to emerge related to the same phenomena, although the structure does not attain a clear shape. These results suggest that the coherent structures derived from the sinusoidal motion are weaker when combined with higher TI, due to an increase in the wake mixing process and a more rapid breakdown of wake structures. At lower frequencies, the wake patterns remain unclear in both cases.

Continuing with the analysis of the signature of the sinusoidal motion on the wake, figure 7 shows the non-dimensionalised power spectral density (PSD) for a probe located at height H and 4.6D downstream the AD. The calculations are limited to the U component and employ the Welch method (Welch, 1967) with a time window of 10 s and a 50% overlap. Both turbulence conditions exhibit peaks associated with the f_{red} defined in table 2, as it was identified by Schliffke et al. (2020, 2024). However, for the HT cases the peaks appear smaller, indicating a more rapid dissipation of the periodic wake structures at

https://doi.org/10.5194/wes-2025-2
Preprint. Discussion started: 11 February 2025

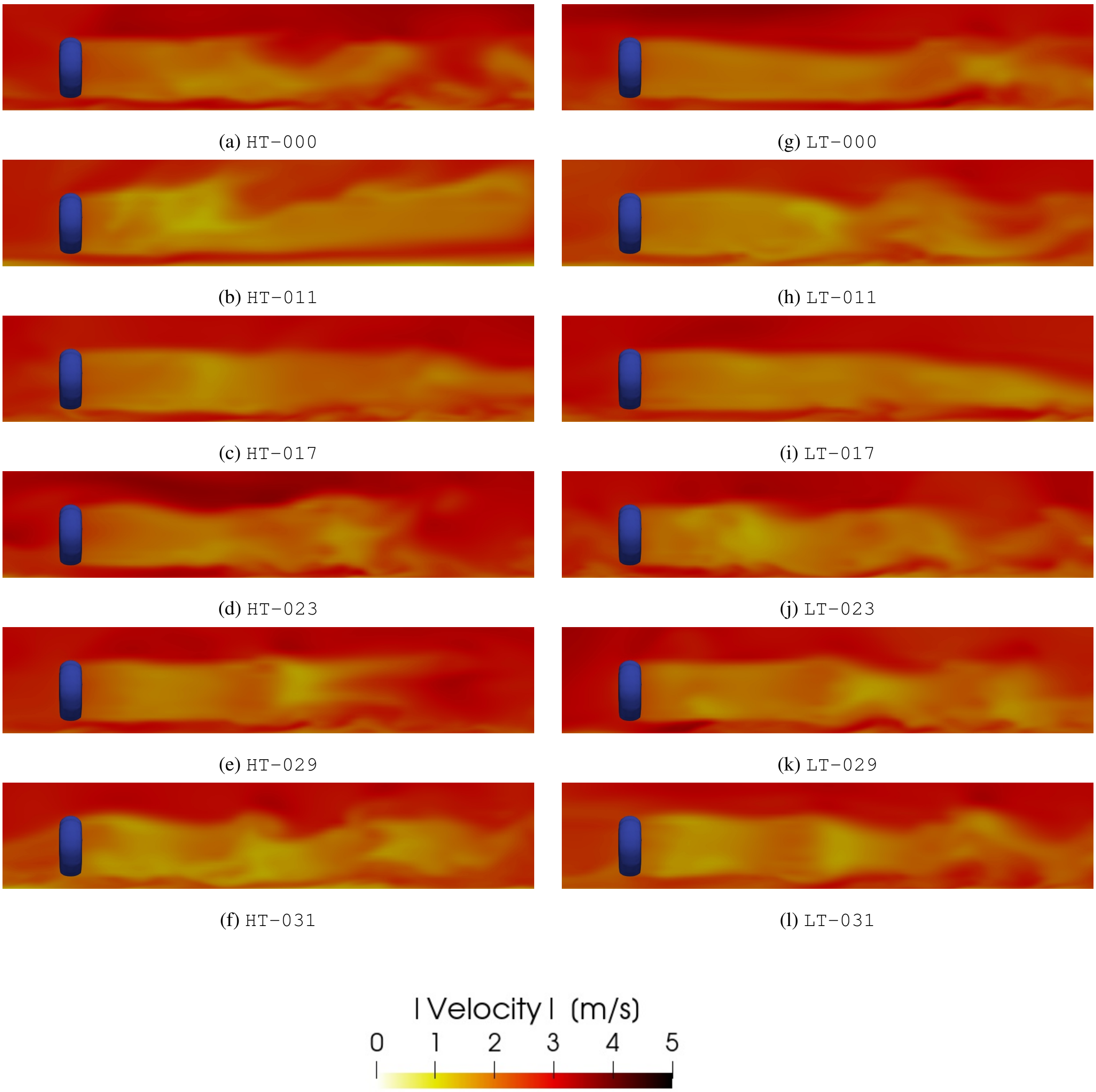

(a) HT-000 (g) LT-000

(b) HT-011 (h) LT-011

(c) HT-017 (i) LT-017

(d) HT-023 (j) LT-023

(e) HT-029 (k) LT-029

(f) HT-031 (l) LT-031

Figure 6. Instantaneous wake velocity magnitude for HT (left) and LT (right) at the final time step of the simulation. A schematic of the AD is included. The cases are named according to table 2.

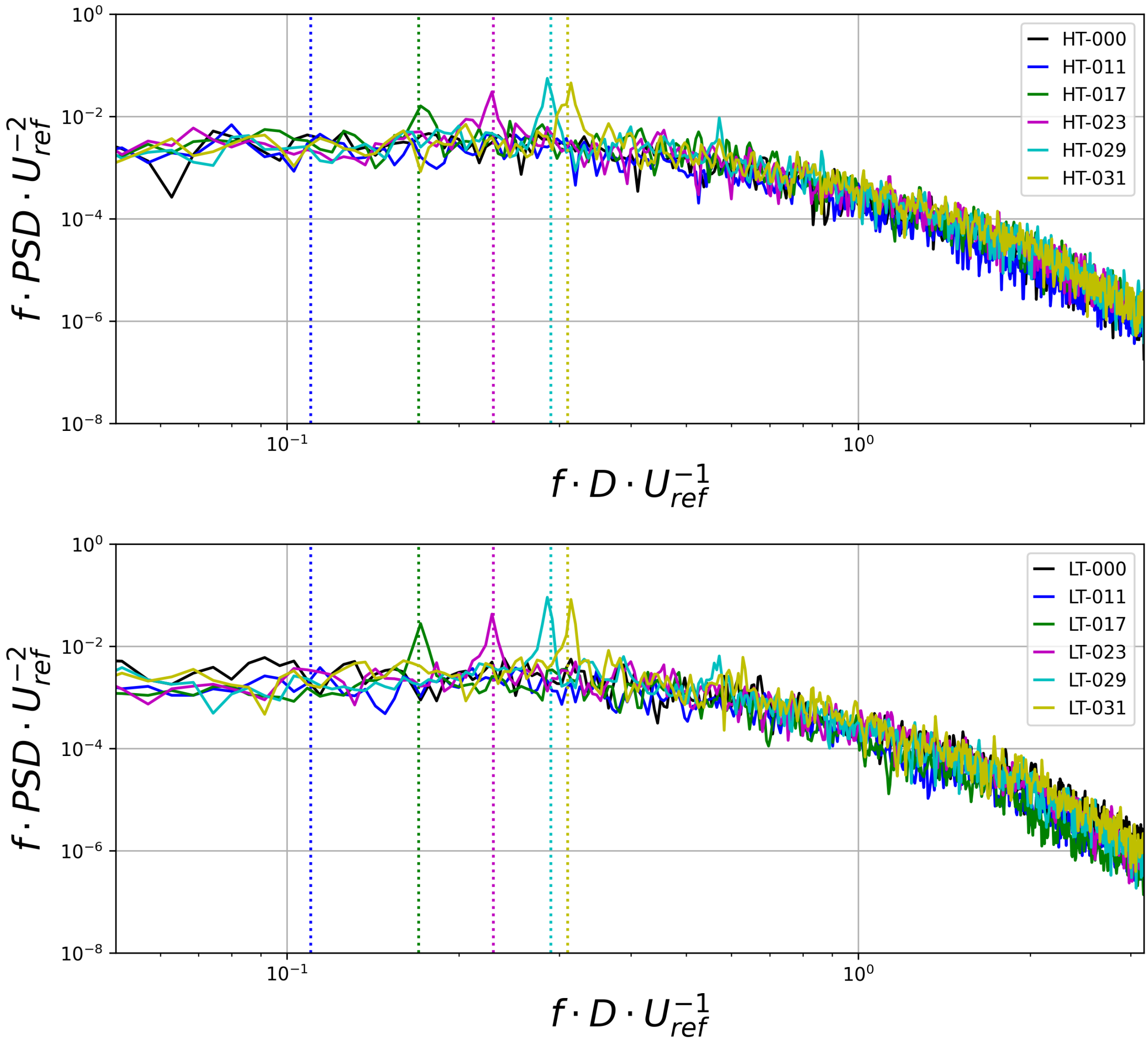

Figure 7. Power spectral density calculated for the U component of a point aligned with the disk axis at $x = 4.6D$. HT (up) and LT (down).

higher TI, as it was observed in figure 6. Also, lower frequencies exhibit no distinguishable peaks, agreeing with the absence of discernible structures in figure 6. In both cases a second peak corresponding to $f_{red} = 0.29$ can be observed, which agrees with the second harmonic of the frequency of the case. This is also observed in the LT case for $f_{red} = 0.31$. Other than that, both cases exhibit no additional significant peaks apart from the surge frequency of the AD. For low TI, the signature in the wake can be distinctly identified for the majority of frequencies as it was done in Schliffke et al. (2020), indicating successful validation of the simulations against experimental data.

https://doi.org/10.5194/wes-2025-2
Preprint. Discussion started: 11 February 2025

eawe european academy of wind energy
Open Access WIND ENERGY SCIENCE DISCUSSIONS

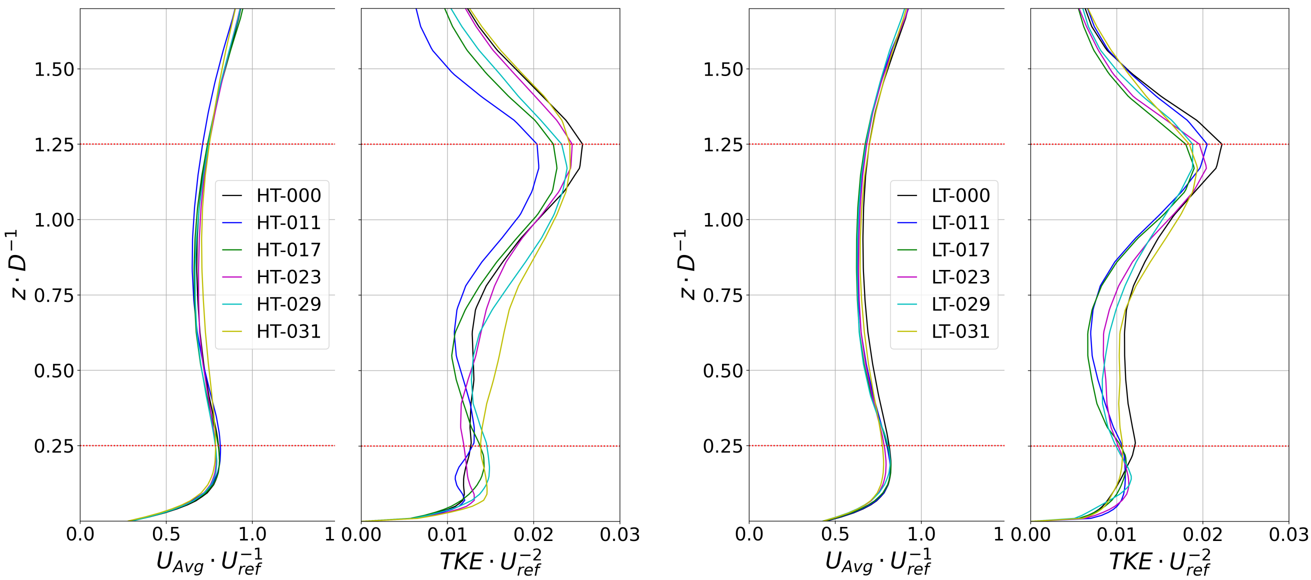

Figure 8. Average Velocity and TKE profiles at 4.6D downstream: HT (left) and LT (right). U_{ref} for each case is the average velocity at hub height measured 5D upstream from the original AD position.

Furthermore, in accordance with the experiments conducted by Schliffke et al. (2020), figure 8 shows the average profiles of velocity and resolved TKE at a downstream distance of 4.6D from the AD under surge motion for all cases in table 2. In this instance, U_{ref} is the hub velocity measured 5D upstream the AD for each case. The results for lower TI exhibit minimal dependence with the frequency, whereas for higher TI, some discrepancies are noted, particularly in the TKE distribution within the wake region. Previous studies (Xu et al., 2023; Schliffke et al., 2020, 2024; Fontanella et al., 2022; Belvasi et al., 2022) have reported no significant differences between frequencies, either in velocity or TKE profiles. In this regard, the method demonstrates strong validation against experiments for low TI, whereas for high TI no research has been conducted under similar conditions.

5 Wake recovery dynamics

To explore the effect of the surge motion on the wake recovery dynamics further, figure 9 depicts the contours corresponding to a wake recovery of 75% of the mean velocity field 5D upstream the AD. While mean wake differences between frequency cases are hardly observed in figure 8, a notable sensitivity to motion frequency in wake length emerges when the full wake profile is taken into account. In both LT and HT conditions, there are cases that differ by up to 1D, either longer or shorter, in comparison to the no motion case. This may suggest that some frequencies give rise to coherence structures that persist longer than others. For the HT case the wake length fluctuates around the no motion case, whereas in the LT all frequencies result in a wake that is larger than the no motion case. This could be associated with the coherence structures persisting for longer in LT cases and dissipating faster in HT cases, as illustrated in section 4. Furthermore, in both cases the wake length corresponding to the

https://doi.org/10.5194/wes-2025-2
Preprint. Discussion started: 11 February 2025

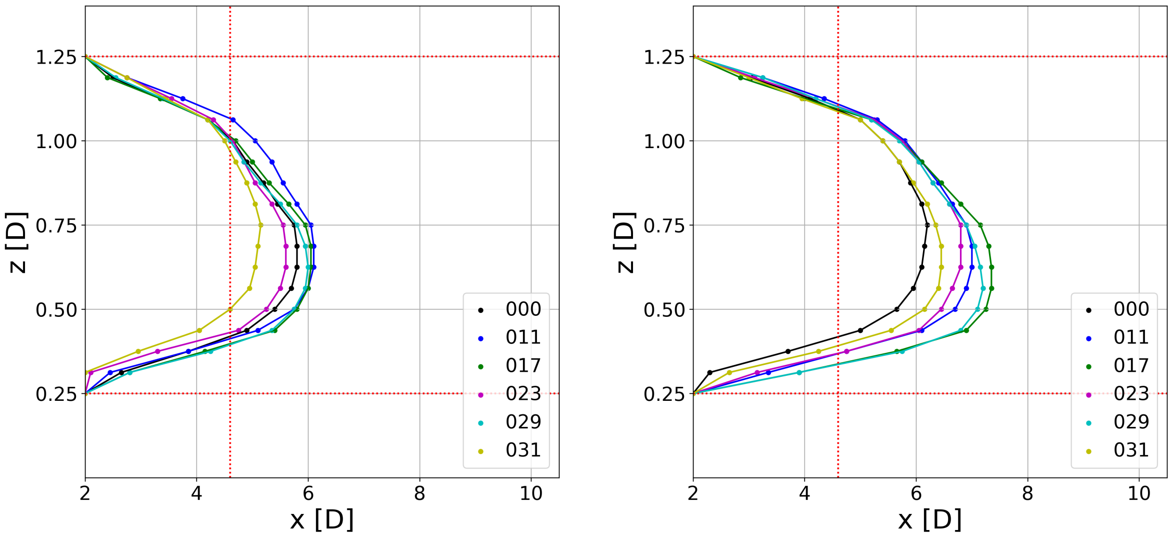

Figure 9. 75% velocity recovery profiles for each case: `HT` (left), and `LT` (right). The AD limits are shown with red dotted lines, along with a line at 4.6D for referencing.

highest frequency 0.31 is the shortest of all moving cases, indicating that in some frequencies the phenomenon increases with frequency up to a point where the tendency reverses. A vertical dotted line at 4.6D indicates the point at which the comparison was made in section 4, thus allowing an understanding of the minimal difference observed between cases at this distance.

For further insights, figure 10 presents the $\pm 5\%$ contours deviating from the 75% one, for the frequencies 0.17 and 0.31. The distance between the contours is calculated by identifying the maximum wake length for the 80% case and drawing a horizontal segment to the 70% contour. A difference in the gradient of wake recovery is observed, which may account for the variation observed in the 75% contours. As detailed in table 3, the variations in length from $L_{-5\%}$ to $L_{+5\%}$ show discrepancies of up to 40% for the same inlet TI. Additionally, it can be seen from figure 10 the altered tendency in wake length with increasing frequency, indicating that the persistence of the wake structures depends on the reduced frequency for both TIs. These results suggest that a more comprehensive analysis is advisable to gain a deeper understanding of the influence of frequency on wake recovery dynamics, and their dependence on ambient turbulence. A full length analysis of the wake would also be beneficial for experimental studies, as the findings align closely with those of experiments conducted on planes at a specific distance from the AD, and none or few studies have looked at the full wake.

6 Conclusions

In this work, a novel CFD method for simulating ABL wind tunnels was proposed. This method was found to be straightforward to configure based on the experimental data obtained from the wind tunnel and it presented a notable reduction in computational cost. The method was compared with the conventional approaches described in the literature and offered an improvement

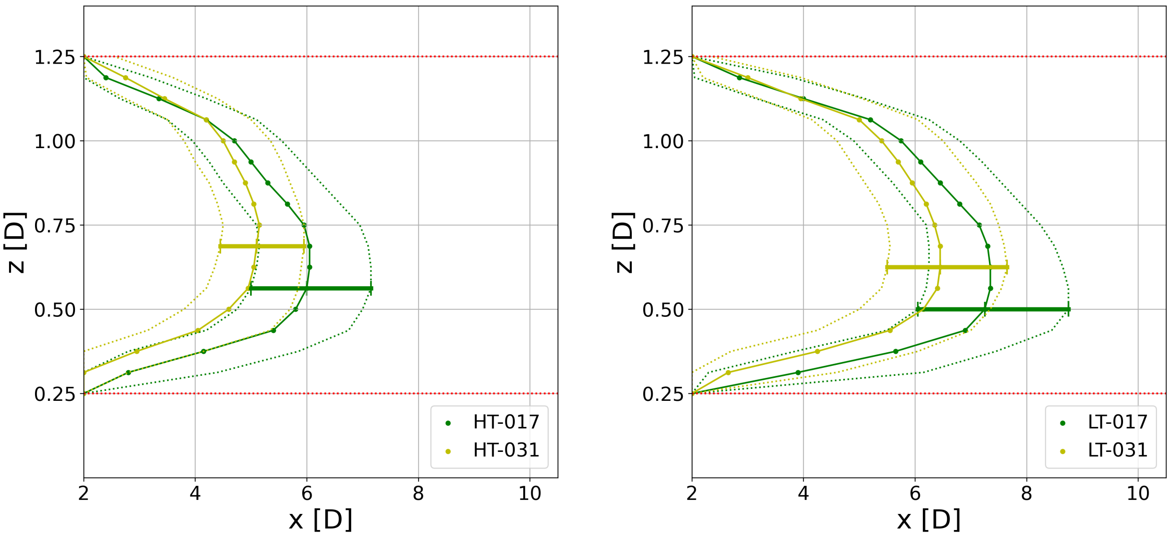

Figure 10. Recovery profiles for 70%, 75% and 80% for reduced frequencies 0.17 and 0.31: HT(left), and LT(right). The AD limits are shown for referencing.

Table 3. Length of the wake velocity contours corresponding to $75\% \pm 5\%$ wake recovery, and length difference. The value is calculated in all cases at the height corresponding to the maximum length of the 80% contour.

Case	$L_{-5\%}$	$L_{+5\%}$	ΔL
HT-017	5.00D	7.15D	2.15D
HT-031	4.45D	5.95D	1.50D
LT-017	6.05D	8.75D	2.70D
LT-031	5.50D	7.65D	2.15D

by avoiding the rapid decay in turbulence quantities. Additionally, the method was subjected to experimental validation by comparing its results with those obtained from ABL wind tunnel experiments. Subsequently, a FOWT model subjected to surge motion was analysed using this technique over a range of frequencies in both low and high turbulence flows. Initially, the expansion and contraction of wake structure was accurately visualized for both inlet conditions, exhibiting patterns in the low TI cases. Subsequently, the PSD was analysed on a probe at 4.6D, where peaks corresponding to the surge motion frequencies were identified for both inlet conditions, although the signal was more discernible in the low turbulence case. Also, the average velocity and TKE profiles at 4.6D were examined, exhibiting analogous behaviour for low turbulence as reported in experimental studies. For high turbulence, the velocity profiles exhibited similar trends, although there were slight discrepancies in the TKE behaviour across different frequencies. Finally, wake recovery was analysed by plotting the 75% wake velocity contour, which revealed that the differences in wake length with respect to the no surge motion case could reach

https://doi.org/10.5194/wes-2025-2
Preprint. Discussion started: 11 February 2025

up to 1D for different frequencies. This was explained by analysing the wake recovery gradient, where differences between different frequencies could reach up to 40% for the same inlet TI, indicating an influence of f_{red} on wake recovery. The surge motion produced longer wakes for all frequency cases in the LT cases, while the HT cases showed a fluctuation of the wake length around the no motion case. A full wake PIV experiment could shed light on this effect, thereby continuing this research in the context of FOWT subjected to surge motion.

Code availability. The SOWFA CFD tool is made available by NREL (https://github.com/NREL/SOWFA/; NREL, 2024). The code developed for the methodology proposed in this work can be made available upon request.

Author contributions. DAB, ADO and SA were responsible for conceptualization and methodology during this research. DAB performed the numerical simulations. SA was responsible for providing the experimental results. The original draft was written by DAB and reviewed and edited by ADO, RS and SA.

Competing interests. One of the co-authors is a member of the editorial board of the journal Wind Energy Science.

Acknowledgements. The authors would like to acknowledge the computational time in the TUPAC cluster, made available by the CSC-CONICET, and École Centrale Nantes for providing the experimental measurements.

Financial support. The authors would like to acknowledge the University of Buenos Aires for the funds received through grant 20620190100001BA. Furthermore, DAB would like to express his gratitude to the 2023 UBAINT Doctoral Program of UBA for the financial support.

https://doi.org/10.5194/wes-2025-2
Preprint. Discussion started: 11 February 2025

References

Aubrun, S., Bastankhah, M., Cal, R., Conan, B., Hearst, R., Hoek, D., Hölling, M., Huang, M., Hur, C., Karlsen, B., Neunaber, I., Obligado, M., Peinke, J., Percin, M., Saetran, L., Schito, P., Schliffke, B., Sims-Williams, D., Uzol, O., Vinnes, M., and Zasso, A.: Round-robin tests of porous disc models, Journal of Physics: Conference Series, 1256, 012 004, https://doi.org/10.1088/1742-6596/1256/1/012004, 2019.

Barthelmie, R., Hansen, O. F., Enevoldsen, K., Højstrup, J., Frandsen, S., Pryor, S., Larsen, S., Motta, M., and Sanderhoff, P.: Ten Years of Meteorological Measurements for Offshore Wind Farms , Journal of Solar Energy Engineering, 127, 170–176, 2005.

Bayati, I., Belloli, M., Bernini, L., and Zasso, A.: Wind Tunnel Wake Measurements of Floating Offshore Wind Turbines, Energy Procedia, 137, 214–222, https://doi.org/https://doi.org/10.1016/j.egypro.2017.10.375, 14th Deep Sea Offshore Wind R&D Conference, EERA DeepWind'2017, 2017.

Belvasi, N., Conan, B., Schliffke, B., Perret, L., Desmond, C., Murphy, J., and Aubrun, S.: Far-Wake Meandering of a Wind Turbine Model with Imposed Motions: An Experimental S-PIV Analysis, Energies, 15, https://doi.org/10.3390/en15207757, 2022.

Bodini, N., Lundquist, J. K., and Kirincich, A.: Offshore Wind Turbines Will Encounter Very Low Atmospheric Turbulence, Journal of Physics: Conference Series, 1452, 012 023, https://doi.org/10.1088/1742-6596/1452/1/012023, 2020.

Calaf, M., Meneveau, C., and Meyers, J.: Large eddy simulation study of fully developed wind-turbine array boundary layers, Physics of fluids, 22, 2010.

Chen, Z., Wang, X., Guo, Y., and Kang, S.: Numerical analysis of unsteady aerodynamic performance of floating offshore wind turbine under platform surge and pitch motions, Renewable Energy, 163, 1849–1870, https://doi.org/https://doi.org/10.1016/j.renene.2020.10.096, 2021.

Chen, Z., Wei, C., Chen, Z., Wang, S., and Tang, L.: Numerical Simulation of Atmospheric Boundary Layer Turbulence in a Wind Tunnel Based on a Hybrid Method, Atmosphere, 13, https://www.mdpi.com/2073-4433/13/12/2044, 2022.

Churchfield, M., Lee, S., Moriarty, P., Martinez, L., Leonardi, S., Vijayakumar, G., and Brasseur, J.: A large-eddy simulation of wind-plant aerodynamics, in: 50th AIAA aerospace sciences meeting including the new horizons forum and aerospace exposition, p. 537, 2012a.

Churchfield, M. J., Lee, S., Michalakes, J., and Moriarty, P. J.: A numerical study of the effects of atmospheric and wake turbulence on wind turbine dynamics, Journal of turbulence, p. N14, 2012b.

Diaz, G. P. N., Saulo, A. C., and Otero, A. D.: Comparative study on the wake description using actuator disc model with increasing level of complexity, Journal of Physics: Conference Series, 1256, 012 017, https://doi.org/10.1088/1742-6596/1256/1/012017, 2019.

Farrugia, R., Sant, T., and Micallef, D.: A study on the aerodynamics of a floating wind turbine rotor, Renewable Energy, 86, 770–784, https://doi.org/https://doi.org/10.1016/j.renene.2015.08.063, 2016.

Feng, C., Gu, M., and Zheng, D.: Numerical simulation of wind effects on super high-rise buildings considering wind veering with height based on CFD, Journal of Fluids and Structures, 91, 102 715, https://doi.org/https://doi.org/10.1016/j.jfluidstructs.2019.102715, 2019.

Fontanella, A., Zasso, A., and Belloli, M.: Wind tunnel investigation of the wake-flow response for a floating turbine subjected to surge motion, Journal of Physics: Conference Series, 2265, 042 023, https://doi.org/10.1088/1742-6596/2265/4/042023, 2022.

Gao, Z., Li, Y., Wang, T., Ke, S., and Li, D.: Recent improvements of actuator line-large-eddy simulation method for wind turbine wakes, Applied Mathematics and Mechanics, 42, 511–526, 2021.

Hodgson, E. L., Andersen, S. J., Troldborg, N., Forsting, A. M., Mikkelsen, R. F., and Sørensen, J. N.: A Quantitative Comparison of Aeroelastic Computations using Flex5 and Actuator Methods in LES, Journal of Physics: Conference Series, 1934, 012 014, https://doi.org/10.1088/1742-6596/1934/1/012014, 2021.

Hubert, A., Conan, B., and Aubrun, S.: Spatio-temporal behavior of the far-wake of a wind Turbine model subjected to harmonic motions: Phase averaging applied to Stereo-PIV measurements, Wind Energy Science Discussions, 2024, 1–25, https://doi.org/10.5194/wes-2024-95, 2024.

Jimenez, A., Crespo, A., Migoya, E., and Garcia, J.: Advances in large-eddy simulation of a wind turbine wake, Journal of Physics: Conference Series, 75, 012 041, https://doi.org/10.1088/1742-6596/75/1/012041, 2007.

Johlas, H. M., Martínez-Tossas, L. A., Schmidt, D. P., Lackner, M. A., and Churchfield, M. J.: Large eddy simulations of floating offshore wind turbine wakes with coupled platform motion, Journal of Physics: Conference Series, 1256, 012 018, https://doi.org/10.1088/1742-6596/1256/1/012018, 2019.

Johlas, H. M., Martínez-Tossas, L. A., Lackner, M. A., Schmidt, D. P., and Churchfield, M. J.: Large eddy simulations of offshore wind turbine wakes for two floating platform types, Journal of Physics: Conference Series, 1452, 012 034, https://doi.org/10.1088/1742-6596/1452/1/012034, 2020.

Lee, H. and Lee, D.-J.: Effects of platform motions on aerodynamic performance and unsteady wake evolution of a floating offshore wind turbine, Renewable Energy, 143, 9–23, https://doi.org/https://doi.org/10.1016/j.renene.2019.04.134, 2019.

Li, Z. and Yang, X.: Resolvent-based motion-to-wake modelling of wind turbine wakes under dynamic rotor motion, Journal of Fluid Mechanics, 980, A48, https://doi.org/10.1017/jfm.2023.1097, 2024.

Li, Z., Dong, G., and Yang, X.: Onset of wake meandering for a floating offshore wind turbine under side-to-side motion, Journal of Fluid Mechanics, 934, A29, https://doi.org/10.1017/jfm.2021.1147, 2022.

Lopez, B., Usera, G., Narancio, G., Mendina, M., Draper, M., and Cataldo, J.: Numerical ABL Wind Tunnel Simulations with Direct Modeling of Roughness Elements Through Immersed Boundary Condition Method, in: Progress in Wall Turbulence 2, edited by Stanislas, M., Jimenez, J., and Marusic, I., pp. 73–82, Springer International Publishing, Cham, 2016.

Messmer, T., Hölling, M., and Peinke, J.: Enhanced recovery caused by nonlinear dynamics in the wake of a floating offshore wind turbine, Journal of Fluid Mechanics, 984, A66, https://doi.org/10.1017/jfm.2024.175, 2024.

Munters, W., Meneveau, C., and Meyers, J.: Turbulent Inflow Precursor Method with Time-Varying Direction for Large-Eddy Simulations and Applications to Wind Farms, Boundary-Layer Meteorology, 159, 305–328, https://doi.org/10.1007/s10546-016-0127-z, 2016.

Nandi, T. N. and Yeo, D.: Estimation of integral length scales across the neutral atmospheric boundary layer depth: A Large Eddy Simulation study, Journal of Wind Engineering and Industrial Aerodynamics, 218, 104 715, https://doi.org/https://doi.org/10.1016/j.jweia.2021.104715, 2021.

Navarro Diaz, G. P., Saulo, A. C., and Otero, A. D.: Wind farm interference and terrain interaction simulation by means of an adaptive actuator disc, Journal of Wind Engineering and Industrial Aerodynamics, 186, 58–67, https://doi.org/https://doi.org/10.1016/j.jweia.2018.12.018, 2019.

Navarro Diaz, G. P., Saulo, A. C., and Otero, A. D.: Full wind rose wind farm simulation including wake and terrain effects for energy yield assessment, Energy, 237, 121 642, https://doi.org/https://doi.org/10.1016/j.energy.2021.121642, 2021.

Navarro Diaz, G. P., Otero, A. D., Asmuth, H., Sørensen, J. N., and Ivanell, S.: Actuator line model using simplified force calculation methods, Wind Energy Science, 8, 363–382, https://doi.org/10.5194/wes-8-363-2023, 2023.

OpenCFD-Ltd: OpenFOAM, https://www.openfoam.com/, accessed: 2024-12-10, 2004.

O'Sullivan, J., Archer, R., and Flay, R.: Consistent boundary conditions for flows within the atmospheric boundary layer, Journal of Wind Engineering and Industrial Aerodynamics, 99, 65–77, https://doi.org/https://doi.org/10.1016/j.jweia.2010.10.009, 2011.

https://doi.org/10.5194/wes-2025-2
Preprint. Discussion started: 11 February 2025

Porté-Agel, F., MENEVEAU, C., and PARLANGE, M. B.: A scale-dependent dynamic model for large-eddy simulation: application to a neutral atmospheric boundary layer, Journal of Fluid Mechanics, 415, 261–284, https://doi.org/10.1017/S0022112000008776, 2000.

Porté-Agel, F., Wu, Y.-T., Lu, H., and Conzemius, R. J.: Large-eddy simulation of atmospheric boundary layer flow through wind turbines and wind farms, Journal of Wind Engineering and Industrial Aerodynamics, 99, 154–168, https://doi.org/https://doi.org/10.1016/j.jweia.2011.01.011, the Fifth International Symposium on Computational Wind Engineering, 2011.

Porté-Agel, F., Bastankhah, M., and Shamsoddin, S.: Wind-Turbine and Wind-Farm Flows: A Review, Boundary-Layer Meteorology, 174, 1–59, https://doi.org/10.1007/s10546-019-00473-0, 2020.

Ramos-García, N., Kontos, S., Pegalajar-Jurado, A., González Horcas, S., and Bredmose, H.: Investigation of the floating IEA Wind 15 MW RWT using vortex methods Part I: Flow regimes and wake recovery, Wind Energy, 25, 468–504, https://doi.org/https://doi.org/10.1002/we.2682, 2022.

Richards, P. and Hoxey, R.: Appropriate boundary conditions for computational wind engineering models using the k-ε turbulence model, Journal of Wind Engineering and Industrial Aerodynamics, 46-47, 145–153, https://doi.org/https://doi.org/10.1016/0167-6105(93)90124-7, proceedings of the 1st International on Computational Wind Engineering, 1993.

Schliffke, B.: Experimental characterisation of the far wake of a modelled floating wind turbine as a function of incoming swell, Ph.D. thesis, École centrale de Nantes, 2022.

Schliffke, B., Aubrun, S., and Conan, B.: Wind Tunnel Study of a "Floating" Wind Turbine's Wake in an Atmospheric Boundary Layer with Imposed Characteristic Surge Motion, Journal of Physics: Conference Series, 1618, 062 015, https://doi.org/10.1088/1742-6596/1618/6/062015, 2020.

Schliffke, B., Conan, B., and Aubrun, S.: Floating wind turbine motion signature in the far-wake spectral content – a wind tunnel experiment, Wind Energy Science, 9, 519–532, https://doi.org/10.5194/wes-9-519-2024, 2024.

Schumann, U.: Subgrid scale model for finite difference simulations of turbulent flows in plane channels and annuli, Journal of computational physics, 18, 376–404, 1975.

Shi, L., Shi, L., and Yeo, D.: OpenFOAM large-eddy simulations of atmospheric boundary layer turbulence for wind engineering applications, US Department of Commerce, National Institute of Standards and Technology, 2016.

Sivalingam, K., Martin, S., and Singapore Wala, A. A.: Numerical Validation of Floating Offshore Wind Turbine Scaled Rotors for Surge Motion, Energies, 11, https://doi.org/10.3390/en11102578, 2018.

Stull, R. B.: An introduction to boundary layer meteorology, vol. 13, Springer Science & Business Media, 2012.

Thordal, M. S., Bennetsen, J. C., Capra, S., and Koss, H. H. H.: Engineering approach for a CFD inflow condition using the precursor database method, Journal of Wind Engineering and Industrial Aerodynamics, 203, 104 210, https://doi.org/https://doi.org/10.1016/j.jweia.2020.104210, 2020.

Tran, T. T. and Kim, D.-H.: A CFD study into the influence of unsteady aerodynamic interference on wind turbine surge motion, Renewable Energy, 90, 204–228, https://doi.org/https://doi.org/10.1016/j.renene.2015.12.013, 2016.

Wang, J., Wang, C., Castañeda, O. D., Campagnolo, F., and Bottasso, C. L.: Large-eddy simulation of scaled floating wind turbines in a boundary layer wind tunnel, Journal of Physics: Conference Series, 1037, 072 032, https://doi.org/10.1088/1742-6596/1037/7/072032, 2018.

https://doi.org/10.5194/wes-2025-2
Preprint. Discussion started: 11 February 2025

Wang, X., Cai, C., Cai, S.-G., Wang, T., Wang, Z., Song, J., Rong, X., and Li, Q.: A review of aerodynamic and wake characteristics of floating offshore wind turbines, Renewable and Sustainable Energy Reviews, 175, 113 144, https://doi.org/https://doi.org/10.1016/j.rser.2022.113144, 2023.

Welch, P.: The use of fast Fourier transform for the estimation of power spectra: a method based on time averaging over short, modified periodograms, IEEE Transactions on audio and electroacoustics, 15, 70–73, 1967.

Xu, S., Zhuang, T., Zhao, W., and Wan, D.: Numerical investigation of aerodynamic responses and wake characteristics of a floating offshore wind turbine under atmospheric boundary layer inflows, Ocean Engineering, 279, 114 527, https://doi.org/https://doi.org/10.1016/j.oceaneng.2023.114527, 2023.

Yi, Z., Wang, L., Li, X., Zhang, Z., Zhou, X., and Yan, B.: Computational Fluid Dynamics-Aided Simulation of Twisted Wind Flows in Boundary Layer Wind Tunnel, Applied Sciences, 14, https://doi.org/10.3390/app14030988, 2024.

Yoshizawa, A.: Statistical theory for compressible turbulent shear flows, with the application to subgrid modeling, The Physics of Fluids, 29, 2152–2164, https://doi.org/10.1063/1.865552, 1986.

Zahn, E. and Bou-Zeid, E.: Correction: Setting Up a Large-Eddy Simulation to Focus on the Atmospheric Surface Layer, Boundary-Layer Meteorology, 190, 19, https://doi.org/10.1007/s10546-024-00865-x, 2024.